



HAL
open science

Experimental and numerical investigation of the response of geocell-reinforced walls to horizontal localized impact

Maxime Soudé, Bastien Chevalier, Michel Grediac, Aurélie Talon, Roland Gourves

► **To cite this version:**

Maxime Soudé, Bastien Chevalier, Michel Grediac, Aurélie Talon, Roland Gourves. Experimental and numerical investigation of the response of geocell-reinforced walls to horizontal localized impact. *Geotextiles and Geomembranes*, 2013, 39, pp.39-50. 10.1016/j.geotexmem.2013.07.006 . hal-00925559

HAL Id: hal-00925559

<https://uca.hal.science/hal-00925559v1>

Submitted on 8 Jan 2014

HAL is a multi-disciplinary open access archive for the deposit and dissemination of scientific research documents, whether they are published or not. The documents may come from teaching and research institutions in France or abroad, or from public or private research centers.

L'archive ouverte pluridisciplinaire **HAL**, est destinée au dépôt et à la diffusion de documents scientifiques de niveau recherche, publiés ou non, émanant des établissements d'enseignement et de recherche français ou étrangers, des laboratoires publics ou privés.

EXPERIMENTAL AND NUMERICAL INVESTIGATION OF
THE RESPONSE OF GEOCELL-REINFORCED WALLS TO
HORIZONTAL LOCALIZED IMPACT

Authors:

Maxime SOUDÉ^{1,2,3}

Bastien CHEVALIER^{2,3}

Michel GRÉDIAC^{2,3}

Aurélien TALON^{2,3}

Roland GOURVÈS¹

Affiliations:

1 Sol Solution Géotechnique Réseaux – 63204 Riom Cedex, France

2 Clermont Université, Université Blaise Pascal, Institut Pascal, BP 10448, F-63000 Clermont-Ferrand, France

3 CNRS, UMR 6602, Institut Pascal, F-63171 Aubière, France

1 Abstract:

2 The aim of this work is to study the effect of a localized impact on a wall made
3 of soil reinforced with geocells. First, two structures were tested with an impacting
4 remote-controlled car. Such experiments, carried out on 1/10th-scale model structures
5 for practical reasons, are designed to mimic the mechanical response of a alveolar
6 geocell reinforcement system. Two types of constitutive materials were considered for
7 the geocells with very different mechanical properties. The test structures were
8 dismantled after the tests to analyse the influence of the impact on the cell layers,
9 especially within their bulk. Examining the video of the tests captured with two high-
10 speed cameras also helped understanding the phenomena that occurred during impact.
11 These experiments were completed by numerical simulations whose objective was to
12 understand more clearly the causes of the phenomena observed either within the
13 dismantled structures or in the videos.

14
15 Keywords: geocell, geotextile, Discrete Element Method, impact load, small-
16 scale model.

17
18
19 **1 INTRODUCTION**

20 The mechanical behaviours of soils reinforced with various types of inclusions
21 such as geosynthetic sheets, steel armatures, geogrids, gabion cells and geocells have
22 attracted attention from many researchers in the recent past (Chen et al., 2013;
23 Moghaddas Tafreshi and Dawson, 2012; Parsons et al., 2009; Saran, 2010; Yang et al.,
24 2012). In particular, the effect of dynamic loads on such structures is a major issue as
25 far as hazard mitigation is concerned. Indeed loadings such as impacts, earthquakes, or
26 blasts, involve complex phenomena that are not clearly understood.

27 For seismic loading, several experimental and numerical studies are available in
28 the literature (Huang et al., 2011; Koseki, 2012; Lee et al., 2010; Leshchinsky et al.,
29 2009; Ling et al., 2009). In addition, standards such as Eurocode 8-5 (Eurocode 8, 2005)
30 take into account the seismic loadings, considering them as additional equivalent static
31 loads , as proposed by the pseudo-static Mononobe-Okabe method (Okabe, 1924;
32 Mononobe and Matsuo, 1929).

33 Concerning the effect of blasts on reinforced soils, the papers which have been
34 published so far mainly deal with numerical studies. Experimental studies are scarce
35 (Chew et al., 2003). This is due to the fact that such experiments are generally risky and
36 need highly specific resources. In addition, they are often performed within the
37 framework of private or military investigations and therefore generally remain
38 unpublished.

39 The case of impact loadings is more and more attractive in the literature though
40 only the case of rockfall embankments has been addressed in practice until now
41 (Nomura, 2002, Bertrand, 2005, Lambert, 2009, Bourrier, 2010, Bourrier, 2011).
42 Furthermore, standards do not really take into account this type of loading because only
43 the deforming capacities of the impacting structure (e.g., a vehicle) are considered in the
44 case of shock rather than those of the impacted structure (Eurocode 1, 1991).

45 In this context, the aim of the present work is to examine the effect of a localized
46 impact on soils reinforced with geocells. Such reinforced structures can potentially be
47 used to protect pre-existing structures against impacts, so this type of study is necessary
48 to investigate their capacity to provide protection.

49 Model tests were carried out instead of full-scale tests. The obvious reason is
50 that they can be much more easily performed compared to full-scale tests, both in terms
51 of cost and safety. In fact, full-scale tests can be considered as a final step of a
52 sustainability study for a given solution. This objective is however out of the scope of

53 the current study. Model tests constitute an essential preliminary stage for observing and
54 understanding qualitatively the mechanisms involved, even in cases where the similarity
55 laws are not satisfied. In the current study, it is too complex to fulfill similitude laws to
56 provide a reliable relationship between model and full-scale responses. In this context,
57 the aim of this study is to investigate the mechanisms involved and to reproduce them
58 using Discrete Element Method (DEM) while assuming that similar behaviours are
59 expected at normal scale. Two impact experiments were first carried out on geocell
60 structures at a scale of $1/10^{\text{th}}$. Two materials featuring very different mechanical
61 properties were chosen for alveolar reinforcement: paper and polymer. These
62 experiments were captured by two high-speed cameras at the same time for thorough
63 investigation of the phenomena occurring during the impacts. The models of reinforced
64 structures were then dismantled and the deformation of the different layers was studied.
65 Finally, numerical simulations were carried out to analyse the global and local
66 mechanisms occurring in the reinforced structures. The results obtained from these
67 experiments and the calculations used are presented and discussed in the different
68 sections of the paper.

69

70 **2 EXPERIMENTAL STUDY**

71 **2.1 Materials and methods**

72 *2.1.1 Details of the test structures*

73 Two reinforced material structures were tested in this study. The difference
74 between these two structures is due to the nature of the reinforcement. Each structure
75 was composed of 19 layers of geocells filled with a specific material. In the horizontal
76 plane, each layer was 120 cm in length, 55 cm in width and 2.5 cm in height (Fig.1).
77 The 3 layers at the bottom of the wall were placed below the ground surface. The total
78 height of this laminated structure was about 47 cm, including the anchoring layers. The

79 whole structure was built up inside a U-shaped wood coffering, which constituted the
80 boundary conditions of the model on three of its sides. This approach is similar to that
81 used by Racana et al. (2003) wherein they have studied the response of similar
82 structures under static loading. The current size of the cells is expected to mimic the
83 response of an M3S® system to the scale of 1/10th. Apart from the cells located in front
84 of the structures which deformed during the filling and compaction stages, the shape of
85 the cells located in the bulk was nearly square, even after compaction.

86 The intercellular bonds were formed by 2 staples placed along the width of the
87 reinforcement strips. After filling, the length of the inner cells along the diagonal was
88 about 5.5 cm. They were square in shape whereas the cells located along the boundary
89 were curved. The boundary conditions were made rigid. Before filling the cells, each
90 layer was pre-extended with a wooden strap structure. After filling, the material was
91 compacted twice: before and after the wooden straps were removed. This process was
92 repeated successively for each additional layer placed on those built beforehand, thus
93 giving rise to the desired model structure.

94

95 *2.1.2 Mechanical properties of the alveolar reinforcement*

96 Two different reinforcements were studied, namely polymer and paper, which
97 were intended to provide very different mechanical responses. The first was an extruded
98 polyethylene film (PE) with a thickness of 0.1 mm. The second was greaseproof paper
99 (GP).

100 Tensile tests were performed on both materials in order to characterize and
101 underline their very different mechanical responses. The initial stiffness and strength
102 were also determined because these quantities are used in the second part of this study
103 dealing with the mechanical model. Two types of specimens were considered for each
104 material: a single strip and two bonded strips. The size of the first type of specimen was

105 25x200 mm². The second type of specimen was made of two strips bonded at
106 midlength. The strips were embedded in compression clamping devices. Tensile tests
107 were conducted with a cross-head speed of 4 mm.min⁻¹. A force transducer and an
108 extensometer were employed to measure the applied tensile force and the global
109 longitudinal elongation of the specimen, respectively. The mean strain and the tensile
110 strength were then deduced from the force/elongation curves.

111 The responses of the different specimens to the tensile tests are shown in Fig.2.
112 For the single strip specimens, it can be observed that the GP specimens exhibit a quasi-
113 linear elastic response with an initial stiffness of 250 kN/m. The PE specimens have
114 response presenting a linear phase with a stiffness of 16 kN/m followed by a yielding
115 phase. Both bonded strip specimens exhibit a plastic response and a force at failure
116 equal to 0.5 kN/mm and 0.25 kN/mm, respectively. Observing the specimens after
117 failure revealed that the strips tore gradually for GP whereas they deformed and
118 plasticized for PE.

119

120 *2.1.3 Fill material*

121 *Definition of the fill material*

122 The fill material used was a mixture made of equal volumes of expanded clay
123 and polystyrene micro-beads. The expanded clay particles presented a sub-spherical
124 shape with diameters ranging from 0.5 to 2.5 mm. The diameter of the polystyrene
125 micro-beads ranged from 0.9 to 1.5 mm. These dimensions are in agreement with those
126 of the cells in terms of ratio between the size of actual fill materials that typically are
127 expected to be used in full-scale structures, and the size of actual cells. Segregation
128 during mixing was avoided by adding 10% in weight of glycerine. This led to a rubbing,
129 light and compressible mixture.

130 Various tests were carried out to characterize the mechanical properties of the
131 fill material, namely oedometric tests, direct shear tests and trench stability tests. These
132 tests were performed with a material density of 450 kg/m^3 , same as that of the fill
133 material in the impact experiments.

134

135 *Young's modulus*

136 An order of magnitude of the Young's modulus was estimated from oedometer
137 tests. The classic equation linking Young's modulus E , oedometric modulus E_{oed} and
138 Poisson's ratio ν was used to estimate the Young's modulus of this material from
139 oedometer tests:

$$E = E_{oed} \frac{(1+\nu)(1-2\nu)}{1-\nu} \quad (1)$$

140 Assuming the value of the Poisson's ratio is known, it is possible to assume a
141 value of the Young's modulus from the value of the oedometric modulus using the
142 above equation. The influence of crushing of the expanded clay particle on Young's
143 modulus was not considered here since this value was used as an order of magnitude
144 only.

145 An average value of the oedometric modulus E_{oed} of 0.6 MPa was obtained. For
146 values of the Poisson's ratio ranging between 0.2 and 0.35, the Young's modulus ranges
147 between 0.4 and 0.55 MPa (Eq. 1).

148

149 *Shear strength characterization*

150 Direct shear tests were performed on circular specimens of 6 cm diameter and
151 2 cm thickness. The shear tests were conducted up to a maximum displacement of 5 mm
152 and with vertical confining pressures between 1.4 and 21.7 kPa. An internal friction
153 angle φ of 44° and a cohesion c of 5 kPa were deduced from these tests. The confining

154 pressure used were lower than those which are likely to appear in the impact
155 experiment, so the friction angle given here should represent a upper limit value.

156

157 *2.1.4 Impacting vehicle*

158 The impact velocity and the geometry of the impacting interface were key-
159 parameters in this experiment. A remote-controlled vehicle was chosen as the impacting
160 device to ensure precise control of the velocity as impact occurred. In addition, a
161 cylindrical steel rod was fixed on the front of the vehicle. This was made to adjust the
162 location of the impact precisely and increase the moment for a given speed.

163 The size of the front rod fitted the size of the cells: diameter $d = 5$ cm and length
164 $L = 18$ cm. Two similar vehicles were prepared: one for each type of reinforced soil
165 structure, since the vehicles were non-reusable after impact. The weight of each vehicle
166 was 5 kg including the front rod. The speed of the vehicle during impact time was set to
167 $10 \text{ m}\cdot\text{s}^{-1}$. The modelled impact is found to be equivalent to a vehicle of 5 tons with a
168 speed of 110 km/h at full scale.

169

170 *2.1.5 High-speed video cameras*

171 Two high-speed video cameras were used to track the vehicles during each
172 impact (Fig.3). Camera Nr.1 was a Fastcam-APX 120K. It captures 1600 frames/second
173 with a sensor resolution of 1024x768 pixels. This camera was placed in such a way that
174 it recorded the impact with an open angle view. It was located 2.5 m above ground
175 level. Camera Nr.2 was a black and white Photron APX 1024x512 pixels placed directly
176 at ground level. It recorded the impact from a lateral viewpoint. Its sensor resolution is
177 the same as that of the other camera but it records 4000 frames/second. Both vehicles
178 were equipped with patched targets on their lateral side to deduce their location,
179 velocity and acceleration in time from footage analysis.

180

181

2.2 Results and discussion

182

2.2.1 Global analysis

183

184

185

186

187

188

189

190

191

192

193

194

195

196

197

2.2.2 Local analysis after impact and dismantling the reinforced

198

structure

199

200

201

202

203

204

205

The readers of the electronic version of this paper are invited to watch the videos available on the website of the Journal. Both videos enable us to observe and analyse each impact. First the rod penetrated into the structure. The distance travelled within the structure was only a few centimetres: 13 cm for the GP reinforced structure and 17.3 cm for the PE one. The deformation spread from the impact zone to the top free boundary by pushing a cone-shaped part of the reinforced structure. This phenomenon is visible in Fig.4. After having reached its maximal penetration, the vehicle moved back slightly and slowly compared to the speed reached just before the impact occurred. It can be noted that despite the rather considerable deformation of the layers, whose vertical deflection reached a few centimetres for both structures, all the layers returned to their initial location and geometry apart from the failed cell walls (see below). Finally, it was observed that this phenomenon was localized since the cells located further from the impact zone, near the lateral walls for instance, did not move.

The structures were dismantled layer by layer after the impact. The topography of each layer was measured by collecting the location of the nodes of a virtual mesh with a pitch of 5 cm in both horizontal directions. These data enabled us to draw cross-sections of the deformed structures along both the vertical and horizontal planes and deduce the internal deformation of the structures. It was assumed here that the compaction of a layer did not affect the vertical location of the ones previously installed. It must be noted that the impacting vehicles were not removed from the

206 reinforced structures after impact. The zones of the structures affected by the impact
207 were clearly identified. Several conclusions can be drawn from this dismantling stage:

- 208 - a Coulomb wedge can be clearly identified. It starts at the impact zone
209 and spreads toward the top free boundary (Fig.4);
- 210 - it is interesting to note that except for the layer located at the level of the
211 impact, the other layers behave as a whole. This is due to the fact that the
212 reinforcement is regularly spatially distributed and spreads the
213 deformation due to the impact within the layers, thus underlining the
214 very positive effect of the reinforcement. This phenomenon is clearer in
215 the PE-reinforced structure than in the GP-reinforced one. It is also
216 interesting to note that this deformation becomes increasingly less in the
217 layers located further from this plane (Fig.5);
- 218 - the layer located at the level of the impact exhibits a specific response. A
219 significant number of failed GP strips (54) were observed, in particular
220 along the impact direction. On the other hand, only 4 polymeric strips
221 failed. The failed strips are located in a zone defined by the black solid
222 lines in Fig.6. These failed strips are nearly symmetrical with respect to
223 the vertical mid-plane of the rod.

224

225 *2.2.3 Penetration, speed and acceleration of the impacting vehicles*

226 It was possible to measure the displacement of the targets placed on the vehicles
227 by processing the videos provided by the lateral high-speed camera. The axis of the
228 camera pointed perpendicularly to the trajectory of the vehicle and focused on the
229 impact zone. In addition, it was placed far enough from the targets. Thus, no corrections
230 were made on the displacement measurements due to view angle. The velocity and the
231 acceleration can thus be obtained by single and double numerical derivation,

232 respectively. Speed vs. time is plotted in Fig.7. It can be seen that the penetration of the
233 impacting vehicle regularly increases for both types of structures up to a maximum
234 value of 18 cm and 14 cm for the GP- and the PE-reinforced structures, respectively.
235 The initial speed is the same for both tests. It rapidly decreases since the impact lasts
236 only approximately 28 ms for the PE- structure and 40 ms for the GP-reinforced
237 structure.

238 This information is also confirmed by the deceleration curves shown in Fig.8.
239 The deceleration peak equals 400 m.s^{-2} for the PE-structure and 700 m.s^{-2} for the GP-
240 reinforced structure.

241 It is also interesting to investigate the evolution of the equivalent force applied
242 by each impacting vehicle to the structure during the impact. This quantity is obtained
243 using Newton's second law, by multiplying the acceleration by the mass of the
244 impacting vehicle. This force is plotted vs. the penetration of the vehicle in Fig.8.

245 It gives an estimate of the global deformability of each structure in dynamic
246 conditions. The response is linear at first in both cases. The maximum force is reached
247 for the PE-reinforced structure: it is 70% greater than that of the maximum force
248 obtained with the GP-reinforced structure. The apparent dynamic stiffness is also
249 greater for the PE-reinforced structure. This result is somewhat surprising since GP is
250 stiffer than PE. This is certainly due to the intercellular bond failure which caused an
251 apparent softening of the structure. This result is consistent with the fact that the GP-
252 reinforced structure exhibits an apparent plastic response for a displacement lying
253 between 75 mm and 160 mm, which is also likely due to the intercellular bond failure.
254 For the PE-reinforced structure, the impact force propagates more easily into the bulk of
255 the whole reinforcement because of the lower number of failures, thus explaining the
256 higher resistance against vehicle penetration.

257

258

2.3 Conclusion

259 Impact tests performed on two different models of reinforced structures are
260 described in this section. Observing the videos obtained with two high-speed cameras
261 enabled us to describe complex phenomena that occurred during the very short time
262 period of the impacts while dismantling the structures after the tests provided useful
263 information on the spatial distribution of the deformation in the bulk of the layers. The
264 objective now is to propose a numerical model that mimics these experiments in order
265 to assess how certain parameters influence the mechanical response of such structures
266 and to complete the experimental observations. This model, after validation, is expected
267 to pave the way for designing real reinforced structures to resist impact loading.

268

269 3 NUMERICAL APPROACH

270 From the observations and characteristics of the small scale impact, numerical
271 models were built using a 2-dimensional Discrete Element Method and particular
272 molecular dynamics (Cundall and Strack, 1979). The behaviour of the reinforced
273 embankment during impact was reproduced qualitatively. The mechanisms involved
274 were observed and compared with those obtained in the experiment. The aim of this part
275 is first to propose a simple model in view to determining the parameters necessary to
276 reproduce the response of the reinforced wall.

277 The reinforced wall was modelled under 2-dimensional conditions by a vertical
278 cross section starting from the front of the wall and ending at the back of the wall, and
279 including the point of impact between the vehicle and the reinforced wall. In this model,
280 the back of the wall was modelled by a perfectly rigid wall condition. The wall itself
281 was modelled by 19 superimposed layers of geocells filled with a soil material.

282

283 3.1 Fill material modelling

284 Different materials were modelled by particles whose diameters ranged from 2
285 mm to 4 mm. The fill material was placed in the cells using a radius expansion method.
286 Particle density was set to 600 kg.m^{-3} and the final void ratio e to a value of 0.33 so that
287 an apparent density of 450 kg.m^{-3} was obtained for the particle assemblies. The
288 experimental fill material was modelled by a homogenized sample of particles
289 presenting a unique set of mechanical parameters. The rheological contact model
290 included linear contact laws of stiffness $k_n = 1.2 \cdot 10^6 \text{ N/m}$ in the normal direction and
291 $k_s = 6 \cdot 10^5 \text{ N/m}$ in the tangential direction. A Coulomb friction criterion of coefficient
292 $\mu = 1$ was used to bound the value of the tangential force. In addition, no cohesion was
293 taken into account. A rolling resistance was also considered in the contact model so that
294 the shear resistance of the samples could be increased. Biaxial tests were conducted on
295 representative sample to get the macro-mechanical properties. A Young's modulus
296 value of $E = 0.5 \text{ MPa}$, a Poisson's ratio of $\nu = 0.20$ and a friction angle of, 24° were
297 obtained. The difference between the friction angle of the numerical sample and
298 experimental material is discussed in Section 3.8.

299 **3.2 Reinforcement material**

300 The modelled reinforcement corresponds to greaseproof paper (GP). It was
301 modelled by a chain of particles of diameter d_{geo} of 1.5 mm, i.e. smaller than the soil
302 particles (Fig.9). Contacts between the chain particles were given an inter-particle
303 cohesion to represent tensile resistance. The behaviour of the GP strips was modelled
304 with an elastic-linear-fragile law. The stiffness and inter-particle cohesion (normal
305 and tangential) were set to fit the elastic part of the response of the experimental strips
306 of raw material. The contact friction coefficient of the chain particles was set to the
307 same value as that of the soil particles.

308 One reinforcement strip crosses the vertical plane chosen for the model several
309 times. Consequently, the physical continuity of the strip material could not be

310 represented in this vertical cross section. Thus a dummy interaction law was considered
311 between the opposite edges of one cell. This interaction was considered mostly to
312 counter the discontinuity of the strips in the vertical plane and then maintain the global
313 stability of the reinforced wall throughout the calculation. It can be written as follows:

$$\begin{aligned} F &= k_{eq}.d && \text{for } d > d_0 \\ F &= 0 && \text{for } d < d_0 \end{aligned} \quad (2)$$

314

315 where d is the distance between the edges of one cell in the modelling plane, d_0 the
316 initial distance between the edges and k_{eq} the stiffness coefficient of the interaction law.

317 Many deformation mechanisms can affect a filled cell, resulting in movements
318 of the fill material and thus different solicitations within the strip. The reinforced wall
319 was modelled here in 2 dimensions here but the mechanisms of deformation of the cells
320 are 3-dimensional. Consequently, it was not possible to predict the deformation
321 mechanisms of the cells from modelling. The choice was made to deduce the value of
322 k_{eq} , from an expansion test in the horizontal plane on an assembly of 9 cells (Fig.10).
323 The 8 peripheral cells were filled with fill material particles. In the centre cell, a single
324 particle was installed and its radius was progressively increased. The force in the chain
325 particles and the radius of the centre cell were computed in order to deduce the value of
326 the stiffness k_{eq} of the interaction law between the reinforcement particles. The
327 parameters of the basic reinforcement model are provided in Table 1.

328

3.3 Impacting vehicle

329 Only the steel ram of the radio-controlled vehicle was modelled as a single
330 cylinder of 5 kg, 5 cm in diameter and 18 cm in length. The horizontal impact speed
331 was 10 m.s⁻¹. The micromechanical parameters are specified in Table 2.

332

3.4 Results

333 The response of the model is mainly assessed in terms of velocity of the
334 impacting vehicle vs. time from the impact beginning on. The experimental curve of the
335 velocity vs. time is plotted in Fig.11 along with its counterpart obtained with the
336 experimental model.

337 It clearly appears that the experimental velocity decreases more quickly than in
338 the numerical model. In other words, the actual deceleration is greater than that
339 predicted by the model. It means that in experimental test, the energy provided by the
340 impact is dissipated more quickly than in the numerical model. It is also worth
341 mentioning that a slope break occurs in the numerical curve at 19 ms. The objective
342 now is to take into account various refinements of this model and to observe whether
343 these changes induce greater deceleration or not.

344

345 **3.5 Environment dissipation**

346 Many DEM users consider an environment dissipation translated by a parameter
347 called α to take all these effects more globally into account. Using such a parameter is
348 convenient, even though actual physical interpretation remains quite obscure in practice.
349 In this case, the unbalanced force of each particle is multiplied by a coefficient lower
350 than one, thus leading to a vanishing unbalanced force. This automatically increases the
351 energy dissipation in the system. It is often recommended to choose a value of 0.3 for
352 this parameter in the case of cyclic dynamics problems such as earthquakes (Itasca,
353 1999). This value can be lower for fast dynamics problems, as in the current case.

354 Several simulations with various values for this parameter ($\alpha = 2.5\%$, 5% , 10% ,
355 20%) were carried out in order to observe its influence on the response of the model.
356 The model used here is the basic model presented above, without any change other than
357 introducing this parameter. The curves obtained are shown in Fig.12.

358 It seems that $\alpha = 5\%$ leads to the best agreement between experimental and
359 numerical responses. This value has the same order of magnitude as that used in studies
360 dealing with dynamics described in the literature (Deluzarche, 2006; Bourrier, 2010),
361 for instance.

362 The strength of this approach is illustrated by this result which shows that taking
363 a correct value for α enables obtaining a numerical model which provides results in
364 agreement with the experimental results. The drawback, however, is that some
365 phenomena are hidden behind this global parameter. Consequently, this makes it
366 difficult to examine the influence of certain parameters that directly influence the
367 response of the structure, thus restricting any further improvement.

368 The idea now is to perform simulations with $\alpha = 0\%$, but with changes compared
369 to the basic model. The objective at this stage is not really to try to obtain a numerical
370 response which is exactly the same as the experimental one, but mainly to examine in
371 turn the influence of various parameters and to see whether they change the response of
372 the reinforced structure in the right direction. The different parameters which are
373 investigated in the following sections are the shape of the impacting vehicle, the
374 presence of a top plate on the box containing the reinforced structure, the stiffness of the
375 springs used to model the through-thickness response of the layers, confinement and
376 rolling resistance.

377

378 **3.6 Enhanced impacting vehicle**

379 A more realistic shape of the impacting vehicle is now considered for the model
380 of the ram, the wheels and their bonds. The modelled masses and gravity centre are
381 equivalent to the experimental car. All particles are bonded as a clump structure.

382 Compared to the preceding model, the idea here is to take into account the
383 junction between the ram and chassis. This junction is in fact an inclined plate. Some

384 preliminary numerical simulations which are not detailed here have shown that the
385 friction coefficient between soil and plate do not really influence the response, so
386 adjusting the value of this parameter is not really an issue. In the numerical model used
387 here, energy dissipation is due to the friction occurring between particles. Other sources
388 of energy dissipation like particle crushing are not considered here. The curve obtained
389 with the numerical model is shown in Fig.13 along with the experimental one.

390 The curve obtained in this case is similar to that of the basic model from 0 to 8
391 ms. From 8 ms on, a first break in the curve appears and the velocity decreases faster, so
392 this goes in the right direction. At about 19 ms, another break in the curve is observed
393 and the velocity decreases less quickly. Comparing this curve with the deformed model
394 vs. time shows that the first break in the slope (at 8 ms) corresponds to the contact
395 between the ram-chassis junction and the reinforced structure (Fig.13, right). The
396 surface which causes internal friction within the soil is suddenly almost doubled, so the
397 penetration resistance increases accordingly.

398

399 **3.7 Enhanced reinforcement model**

400 **3.7.1 Influence of the top plate**

401 In the model described in section 2, it is explained that a plate was placed at the
402 top of the frame in order to improve the rigidity of boundary conditions. One may
403 wonder whether this plate hinders the vertical movement of the Coulomb wedge and if
404 this affects the velocity curve. A horizontal plate was therefore added at the top of the
405 impacted structure and a simulation was carried out with this model. This plate was
406 modelled by a series of grains and springs, their equivalent mechanical properties being
407 those of a steel plate with the stiffness of the real one. The curve obtained in this case is
408 shown in Fig.14.

409 From 0 to 19 ms, the horizontal velocity is the same as that obtained with the
410 basic model but it keeps decreasing up to about 35 ms. Consequently the break in slope
411 observed with the basic model at about 19 ms is caused by the movement of the
412 Coulomb wedge. Before 19 ms, the weight of this wedge contributes to the deceleration
413 of the impacting vehicle and it is clear that removing this wedge if no plate is placed at
414 the top of the model immediately causes the penetration resistance to decrease, and thus
415 the deceleration to decrease, too. In conclusion, it can be said that the top plate has a
416 significant impact on the velocity curve after $t = 19$ ms, so it must be taken into account
417 in the numerical model.

418

419 3.7.2 *Enhanced reinforcement*

420 There are two main solutions to increase the resistance opposed to the lifting of
421 the Coulomb wedge due to the impact. The first consists in increasing the density of the
422 particles and therefore the mass of the corner. However, since this parameter was fixed
423 during the experiments, this solution could not be considered. The second solution
424 consists in adding a vertical reaction to the reinforcement in the direction opposite to the
425 displacement of the layers. An additional load was then considered to take into account
426 the anchor effect of each layer that could obviously not be modelled in 2 dimensions.
427 This solution is investigated here.

428 As shown in section 2, the reinforced layers located above the impact level were
429 seen to rise as the impact occurred. This rise was greater in the centre cross-section, i.e.
430 close to the impact point, and progressively decreased towards left and right boundaries
431 until a total vanishing at the lateral edges (Fig.15).

432 Tension in the strips appeared due to the deformation resulting from the relative
433 displacement between the anchoring zones and central zone. The model was thus
434 enhanced by adding in each layer a vertical effort in the opposite direction of the

435 vertical displacement of the layer d_y , i.e. downward as the layers were lifted upwards
 436 during impact. The additional force was modelled by the action of linear springs
 437 (Fig.15) located on each side of the central zone and with an initial length l_i and a
 438 stiffness k_i . For an upward displacement of a given layer, the restoring force F_{Vi} can be
 439 written as follow:

$$F_{Vi} = 2 \cdot \sin\left(\arctan\left(\frac{d_y}{l_i}\right)\right) \cdot k_i \cdot \left(\sqrt{l_i^2 + d_y^2} - l_i\right) \quad (3)$$

440 The objective of adding the interaction law was to evaluate its influence on the
 441 accuracy and on the improvement of the basic model. Consequently, the initial lengths l_i
 442 of the interaction springs were deduced from the image analysis of the experimental
 443 results.

444 The spring stiffness k_i was deduced from extension tests modelled by the
 445 reinforced layer in the horizontal plane. The stiffness depends on the length of the layer
 446 tested, so that for a given vertical displacement of one layer during impact, the longer
 447 the spring, the greater the interaction force.

448 The maximal vertical force F_{Vmax} corresponds to the lowest lifted alveolar layer
 449 with an equivalent spring of stiffness $k_1 = 20 \cdot 10^3 \text{ N.m}^{-1}$ and initial length $l_1 = 8 \text{ cm}$ (hard
 450 case). The minimal vertical effort F_{Vmin} corresponds to the highest lifted alveolar layer
 451 with an equivalent spring of stiffness $k_{11} = 5 \cdot 10^3 \text{ N.m}^{-1}$ and initial length $l_{11} = 23 \text{ cm}$
 452 (soft case).

453 Vertical restoring springs were added in the reinforcement model. All the
 454 restoring springs were given the same stiffness value: k_l for the hard case and k_{ll} for the
 455 soft case. The results obtained are shown in Fig.16.

456 In both cases, the difference with the basic model is small in terms of vehicle
 457 velocity vs. time. A close inspection of the images obtained from the simulation shows,
 458 however, that the vertical displacement of the alveolar layers is strongly influenced by

459 the stiffness of these springs. The fill material escaped from the alveoli in the case of
460 stiff springs. This phenomenon is illustrated in Fig.17, where the dotted line represents
461 the upper layer for both the stiff and the soft springs. In conclusion, it seems logical that
462 the penetration resistance due to the Coulomb wedge remains the same as that obtained
463 for the basic model.

464 **3.8 Enhanced soil model**

465 Modelling of granular media as a set of cylindrical (2D) or spherical (3D)
466 particles leads to high rotational mobility of particles (Iwashita et al., 1998; Jiang et al.,
467 2005) resulting in a reduction of the possible values of the macroscopic friction angle.
468 In our case, the friction angle of the fill material equal to 24° , instead 40° in the
469 experiments. Particle shape improvement (Salot et al., 2009; Szarf et al., 2011;
470 Chevalier et al., 2012) and rolling resistance (Iwashita et al., 1998; Jiang et al., 2005)
471 can be used to offset this effect. In this study, the rolling resistance law developed by
472 Jiang and al. (2005) was used. Only the general principles of the rolling resistance law
473 are presented here. A more detailed description of this model can be found in the
474 reference above.

475 Jiang's law consists in applying a moment M to particles in the direction
476 opposing that of the total relative rotation θ_R of the system considered, i.e. {particle-
477 particle} or {particle-wall}. The law can thus be represented by the moment - rotation
478 relation. Physically, Jiang's model is equivalent to considering that particles present a
479 flat surface in the contact zone (Fig.18). The width of the flat surface depends on the
480 shape parameter δ , which is the only parameter of the law. The moment M can thus be
481 deduced from the dummy geometry of the contact using total relative rotation δ . The
482 threshold values M_0 and θ_{R0} depend on the contact properties and forces and their
483 expressions are defined as follows (Jiang et al., 2005):

$$\theta_{R0} = \frac{2F_n}{k_n r \delta} \quad (4)$$

$$M_0 = \frac{1}{6} F_n r \delta \quad (5)$$

484 where k_n the normal contact stiffness, F_n the normal component of contact force, δ the
 485 shape parameter.

486 The case where $\delta = 0$ corresponds to the free rolling particles and the case where
 487 $\delta \rightarrow \infty$ to blocked rotations.

488 The values of the shape parameter δ and the corresponding macroscopic friction
 489 angle are summarized in Table 3. Young's modulus and Poisson's ratio were not
 490 modified by the shape parameter δ .

491 Soils with different macro-mechanical friction angles were modelled to estimate
 492 the influence of this parameter on the mechanical response. The macro-mechanical
 493 friction angle was increased using the rolling resistance law. The other parameters
 494 characterizing the model remain the same as those chosen for the basic simulation (R1
 495 and II). The corresponding curves are shown in Fig.19.

496 Strong influence of the friction angle can be observed. The greater the friction
 497 angle, the greater the deceleration, which is here the objective: to reflect the
 498 experimental response. It is also noteworthy that the break in the slope at 19 ms is still
 499 visible in all cases. It must however be pointed out that a computation time
 500 approximately 4 times greater than that needed for the basic simulation was required to
 501 perform each of these simulations.

502

503 **3.9 Conclusion**

504 In conclusion of the simulations presented above, it can be said that the shape of
505 the ram-chassis, the upper plate placed on the model and the friction angle have a
506 significant influence on the velocity curve vs. time, whereas the confinement and
507 rigidity of the springs modelling the link between the layers have almost no influence.
508 The objective now is to combine all these effects to try to obtain a numerical response
509 that better matches the velocity curve of the experimental response.

510

511 **4 CONCLUSION**

512 This paper presents study of the effect of impacts on a soil wall reinforced with
513 geocells based on experimental and numerical results.

514 Two impact experiments at a one-tenth scale were carried out on geocell
515 structures. Two materials with very different mechanical properties were chosen for the
516 alveolar reinforcement: paper (stiff-fragile mechanical response) and polymer
517 (significant strain at failure). The mechanical properties of these materials were
518 characterized with tensile tests. The fill material was a mixture of expanded clay beads
519 and polystyrene micro-beads. Glycerine was added to this mixture to avoid segregation
520 during mixing. The size and the density of this model fill material match the
521 experimental fill material well. These experiments provided better understanding of
522 geocell wall behaviour during impact and the parameters that influence this behaviour.

523 Based on these experiments a numerical model using a 2-dimensional discrete
524 method and particular molecular dynamics was proposed. This numerical model gives
525 results which are similar to those provided by the paper experiment model. A vertical
526 cross-section of the wall was modelled starting at the front of the wall and ending at its
527 rear. A basic reinforcement model was built and then progressively modified to improve
528 the initial model. These improvements dealt with: (1) introducing a pull-back force on
529 each layer, representing the influence of the missing dimensions of the model, (2)

530 changing the shape of the impacting vehicle and, (3) increasing the shear strength of the
531 fill material.

532 Although a difference between numerical and experimental results could be
533 observed, it was possible to predict qualitatively the global kinematics response of the
534 wall. The different improvement approaches showed that the main difficulty was to
535 obtain a sufficient level of energy dissipation in the model, especially in the 2-
536 dimensional discrete model involving spherically shaped particles. Increasing the shear
537 strength of the fill material narrowed the difference between the experimental and
538 numerical results. It would also be interesting to address the problem of particle
539 crushing in further work because it certainly influences the mechanical behaviour.

540 The effect of broadly used local damping in the model showed that it is possible
541 to obtain good results as soon as the local damping value is well chosen. The dissipation
542 of energy in the numerical modelling is not as important in the experimental test,
543 revealing that some mechanisms still remain unclear and then not reproduced by the
544 model. The local damping can be used to counterbalance this difference, as long as its
545 influence on the modelling results is clearly known. In addition, the value of local
546 damping coefficient should be taken as low as possible since its physical significance is
547 difficult to explain, especially in dynamic testing.

548 Now that important parameters were identified, future work will focus on
549 refining the numerical analysis by modelling a wall in three dimensions and then
550 moving on to full-scale experiments.

551

552 **5 REFERENCES**

553 Bertrand, D., Nicot, F., Gotteland, Ph., Lambert, S., 2005. Modelling a geo-
554 composite cell using discrete analysis. *Computers and Geotechnics*. 32(8), 564-577.

555 Bourrier, F., Nicot, F., Eckert, N., Darve, F., 2010. Comparing numerical and
556 experimental approaches for the stochastic modeling of the bouncing of a boulder on a
557 coarse soil. *European Journal of Environmental and Civil Engineering*. 14(1), 87-111.

558 Bourrier, F., Lambert, S., Heymann, A., Gotteland, P., Nicot, F., 2011. How
559 multi-scale approaches can benefit the design of cellular rockfall protection structures
560 *Canadian Geotechnical Journal*, 48(12), 1803-1816.

561 Chen, R.-H., Huang, Y.-W., Huang, F.-C., 2013. Confinement effect of geocells
562 on sand samples under compression. *Geotextiles and Geomembranes*. 37, 35-44.

563 Chevalier, B., Combe, G., Villard, P., 2012. Experimental and discrete element
564 modeling studies of the trapdoor problem: influence of the macro-mechanical frictional
565 parameters. *Acta Geotechnica*. 7, 15-39.

566 Chew, S.H., Tan, S.A., Karunratne, G.P., Chiew Chiat, N.G., 2003. Performance
567 of geosynthetic reinforced soil wall subject to blast loading: Experimental and
568 numerical study, in: Ling H.I., Leshchinsky D., Tatsuoka F. (Eds), *Reinforced soil
569 Engineering: Advances in research and practice*. CRC Press, Boca Raton, pp. 363-393.

570 Cundall, P.A., Strack, O.D.L., 1979. A discrete numerical model for granular
571 assemblies. *Geotechnique*. 29, 47-65.

572 Deluzarche, R., Cambou, B., 2006. Discrete numerical modeling of rockfill
573 dams. *International Journal for Numerical and Analytical Methods in Geomechanics*.
574 30(11), 1075-1096.

575 Eurocode 1, 1991. *Actions on structures - Part 1-7: Accidental actions from
576 impact and explosions*.

577 Eurocode 8, 2005. Eurocode 8: Design of structures for earthquake resistance -
578 Part 5: Foundations, retaining structures and geotechnical aspects, pp. 32-35.

579 Huang, C.C., Horng, J.C., Chang, W.J., Chiou, J.S., Chen, C.H., 2011. Dynamic
580 behavior of reinforced walls - Horizontal displacement response. *Geotextiles and*
581 *Geomembranes*. 29, 257-267.

582 Itasca, 1999. PFC2D, Theory and background. Itasca Eds.

583 Iwashita, K., Oda, M., 1998. Rotational resistance at contacts in simulation of
584 shear band development by DEM. *Journal of Engineering Mechanics*. 124(3), 285-292.

585 Jiang, M.J., Yu, H.S., Harris, D., 2005. A novel discrete model for granular
586 material incorporating rolling resistance. *Computers and Geotechnics*. 32(5), 340-357.

587 Koseki, J., 2012. Use of geosynthetics to improve seismic performance of earth
588 structures. *Geotextiles and Geomembranes*. 34. 51-68.

589 Lambert, S., Gotteland, P., Nicot, F., 2009. Experimental study of the impact
590 response of geocells as components of rockfall protection embankments. *Natural*
591 *Hazards and Earth System Sciences*. 9, 459-467.

592 Lee, K.Z.Z., Chang, N.Y., Ko, H.Y., 2010. Numerical simulation of
593 geosynthetic-reinforced soil walls under seismic shaking. *Geotextiles and*
594 *Geomembranes*. 28, 317-334.

595 Leshchinsky, D., Ling, H.I., Wang, J.P., Rosen, A., Mohri, Y., 2009. Equivalent
596 seismic coefficient in geocell retention systems. *Geotextiles and Geomembranes*. 27(1),
597 9-18.

598 Ling, H., Leshchinsky, D., Wang, J., Mohri, Y., Rosen, A., (2009). Seismic
599 Response of Geocell Retaining Walls: Experimental Studies. *Journal of Geotechnical*
600 *and Geoenvironmental Engineering*. 135(4), 515-524.

601 Moghaddas Tafreshi, S.N., Dawson, A.R., 2012. A comparison of static and cycli
602 loading responses of foundations on geocell-reinforced sand. *Geotextiles and*
603 *Geomembranes*. 32, 55-68.

604 Mononobe, N., Matsuo, O., 1929. On the determination of earth pressure during
605 earthquakes, in: *Proceeding of the World Engineering Congress, Vol.9, Tokyo (Japan)*,
606 pp.176–182.

607 Nomura, T., Inoue, S., Fuchigami, M., Yokota, Y., Kubo, T., Tatta, N., Arai, K.:
608 Experimental research of reinforced soil wall for rock-fall protection, in: 7th
609 International conference on geosynthetics, Nice, France, 22–27 September, 303–308
610 2002.

611 Okabe, S., 1924. General theory on earth pressure and seismic stability of
612 retaining walls and dams. *Journal of the Japan Society of Civil Engineering*. 10(6),
613 1277–1323.

614 Parsons, R.L., Pokharel, S., Han, J., Halahmi, I., Leshchinsky, D., 2009.
615 Behavior of geocells-reinforced granular bases under static and repeated loading. In:
616 Iskander, M., Laefer, D.F., Hussein, M.H. (Eds) *Contemporary Topics in Ground*
617 *Modification, Problem Soils and Geo-support*, ASCE, 409-416.

618 Racana, N., Grédiac, M., Gourvès, R., 2003. Pull-out response of corrugated
619 geotextile strips. *Geotextiles and Geomembranes*. 21(5), 265-288.

620 Salot, C., Gotteland, P., Villard, P., 2009. Influence of relative density on
621 granular materials behavior: DEM simulations of triaxial tests. *Granular Matter*. 11(4),
622 221-236.

623 Saran, S., 2010. *Reinforced soil and its engineering applications*, Second edition,
624 IK International Publishing.

625 Szarf, K., Combe, G., Villard, P., 2011. Polygons vs. clumps of discs: a
626 numerical study of the influence of grain shape on the mechanical behaviour of granular
627 materials. Powder Technology. 208(2), 279-288.

628 Yang, X., Han, J., Pkharel, S.K., Manandhar, C., Parsons, R.L., Leshchinsky, D.,
629 Halahmi, I., 2012. Accelerated pavement testing of unpaved roads with geocells-
630 reinforced sand bases. Geotextiles and Geomembranes. 32, 95-103.

631

632 Figure caption list:

633 Fig.1 – Diagram of the experimental reinforced wall

634 Fig.2 – Results of tensile tests on single and bonded strips of GP and PE

635 Fig.3 – Views of the experimental site showing the location of the tested walls and the
636 high-speed cameras

637 Fig. 4 – Vertical cross section diagrams of the wall showing the deformation after
638 impact

639 Fig. 5 – Deformation of the front face of the PE wall for the layer located at impact
640 level (top view)

641 Fig. 6 – Location of broken bonds for the GP wall, in the layer located at impact level

642 Fig.7 – Penetration length and vehicle speed versus time for both the GP and the PE
643 walls

644 Fig.8 – Acceleration and unbalanced force on impacting vehicle versus time for both the
645 GP and the PE walls

646 Fig. 9 – Diagram showing the numerical model used for the reinforcement strips

647 Fig. 10 – Diagram showing the principle of the numerical expansion test on filled cells

648 Fig. 11 – Comparison of vehicle velocity versus time for the experimental wall (GP)
649 and basic numerical model

650 Fig. 12– Influence of the local damping coefficient used in the basic numerical model
651 on the response of the wall in terms of vehicle velocity versus time

652 Fig. 13– Vehicle velocity versus time for the basic model, the enhanced vehicle model
653 and the experimental test

654 Fig. 14 – Vehicle velocity versus time for the basic model, the top plate model and the
655 experimental test

656 Fig. 15 – Enhanced model for the reinforcement strips

657 Fig. 16 – Vehicle velocity versus time for the experimental test, the basic numerical
658 model and the improved reinforcement models (soft and hard cases)

659 Fig. 17 – Cross-section of the modelled wall in the case of the improved reinforcement
660 model with soft stiffness (left) and hard-stiffness (right) springs. The dotted line
661 represents the top boundary of the reinforcement strip during impact

662 Fig.18 – Description of the rolling resistance model of Jiang et al. (2005)

663 Fig. 19 –Effect of rolling resistance on the vehicle velocity versus time for the basic
664 case and for the rolling resistance case
665

666 Table 1. Physical and micromechanical parameters of the reinforcement

ρ_{GEO} [kg/m ³]	r_{GEO} [mm]	$k_{n,GEO} = k_{s,GEO}$ [N/m]	$n_{b,GEO} = s_{b,GEO}$ [N/m]	μ_{GEO} [-]	k_{eq} [N/m]
300	0,75	$3.33 \cdot 10^8$	45	1.0	$3 \cdot 10^5$

667

668 Table 3. Physical and micromechanical parameters of the impact loading

ρ_{IMP} [kg/m ³]	r_{IMP} [mm]	$k_{n,IMP} = k_{s,IMP}$ [N/m]	μ_{IMP} [-]	v_{IMP} [m.s ⁻¹]	h_{IMP} [cm]
1,41.10 ⁴	25	10 ¹⁰	1,0	10	17,5

669

670

671 Table 1. Values of shape parameter and macroscopic friction angle

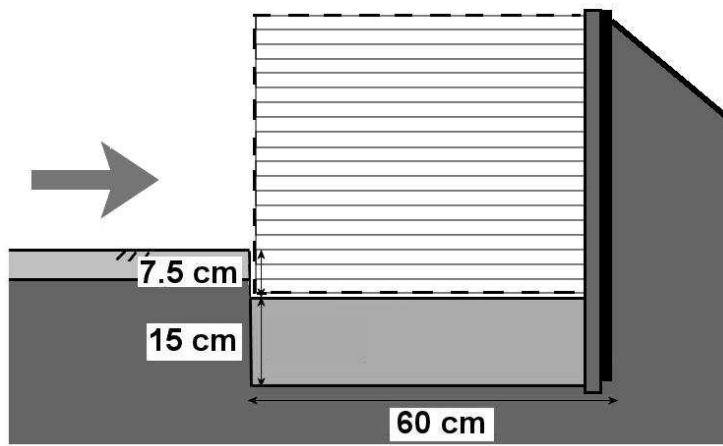
δ	$\varphi_{sol} [^\circ]$
0	24
0,2	26
0,4	28
0,6	31
0,8	33
1,0	35
2,0	43,5
∞	52

672

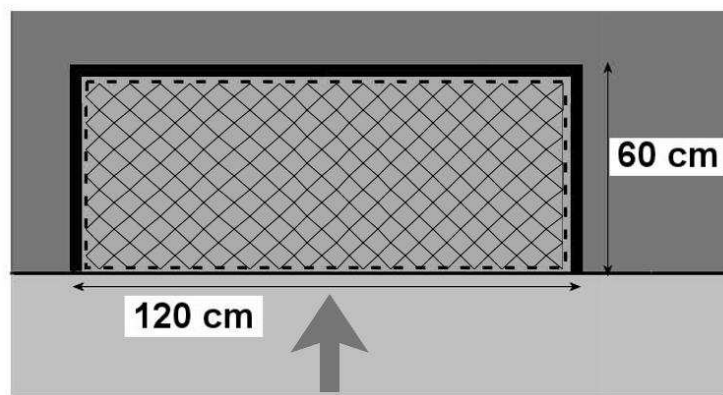
673

674 Fig.1 – Diagram of the experimental reinforced wall







675



vertical cross section



top view

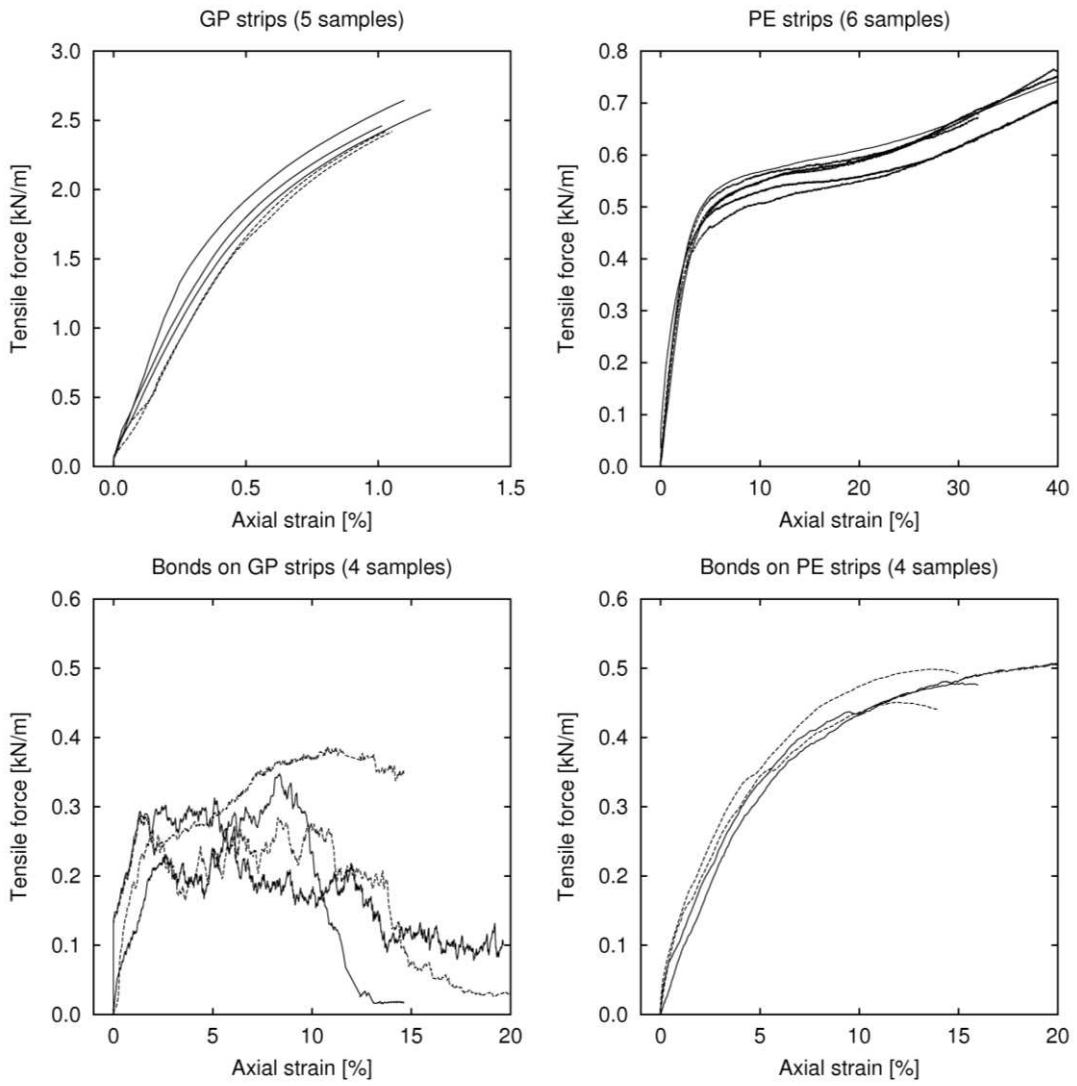
-  tarmac road
-  compacted sand layer
-  location of reinforced wall
-  on-site natural soil
-  outer coffering wood
-  impact direction

676

677

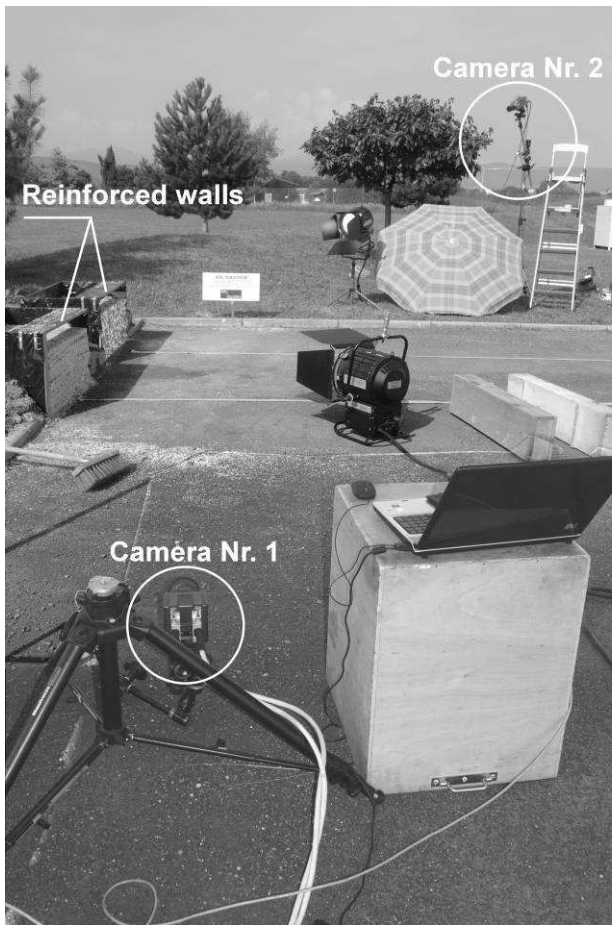
678
679

Fig.2 – Results of tensile tests on single strips and bonded strips of GP and PE.



680
681

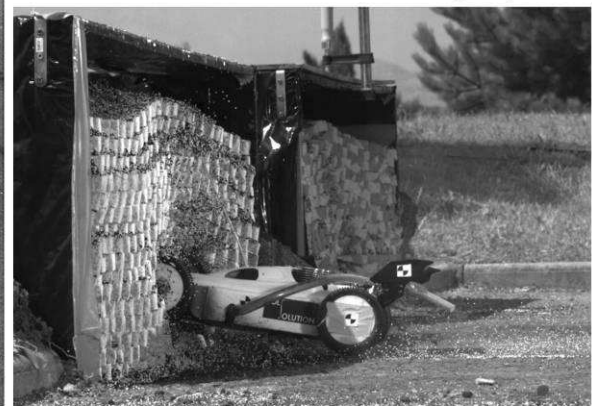
682 Fig.3 – Views of the experimental site showing the location of the tested walls and the
683 high speed cameras
684



Overview on the experimental site



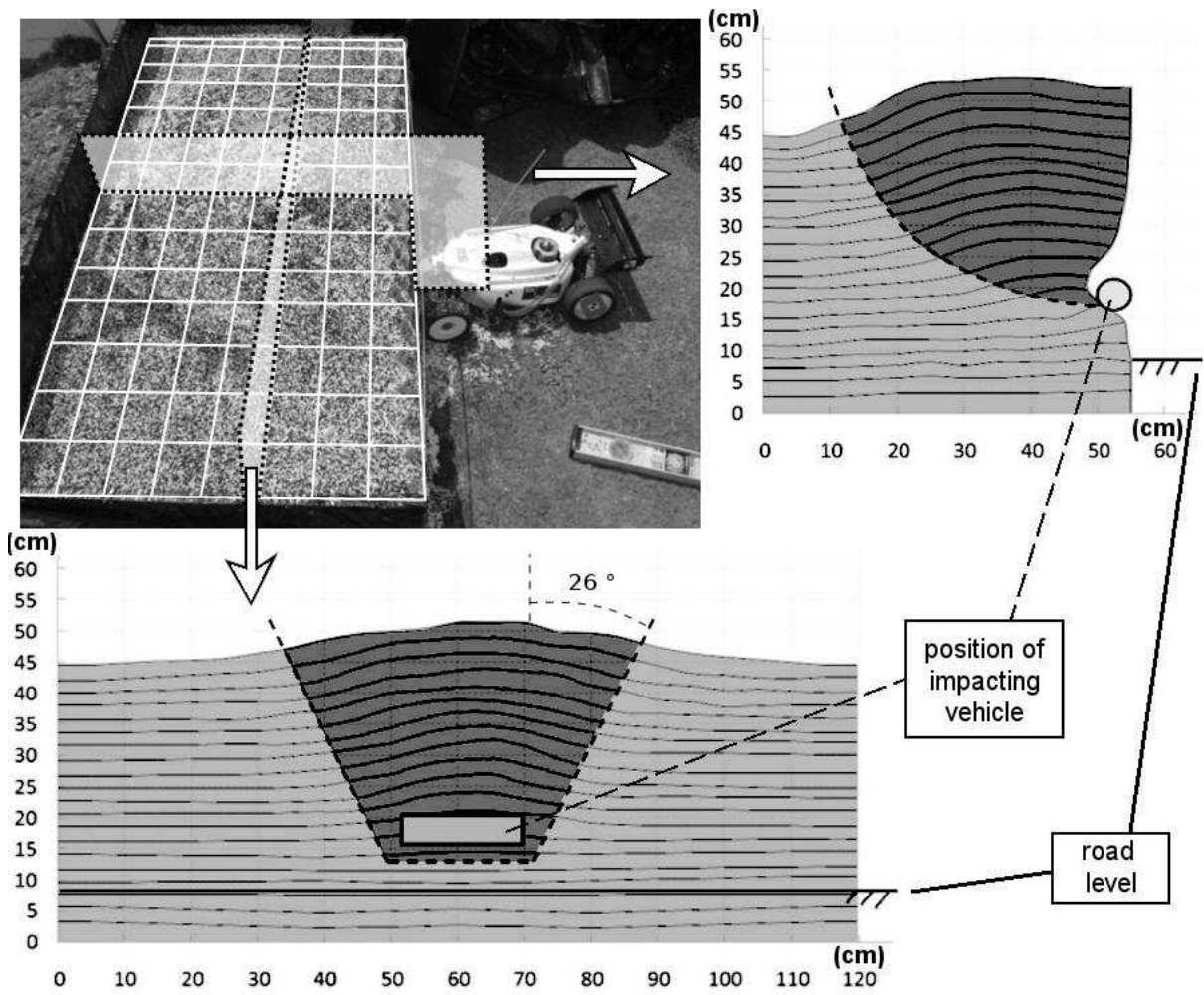
View from Camera Nr.2 during impact



View from Camera Nr.1 during impact

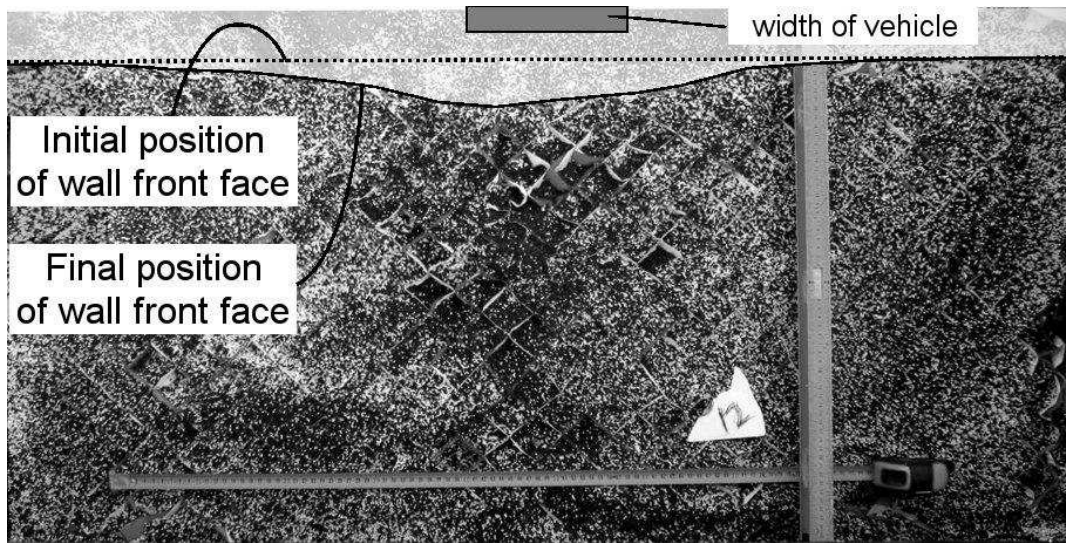
685
686

687 Fig. 4 – Vertical cross section diagrams of the wall showing the deformation after
688 impact
689



690
691

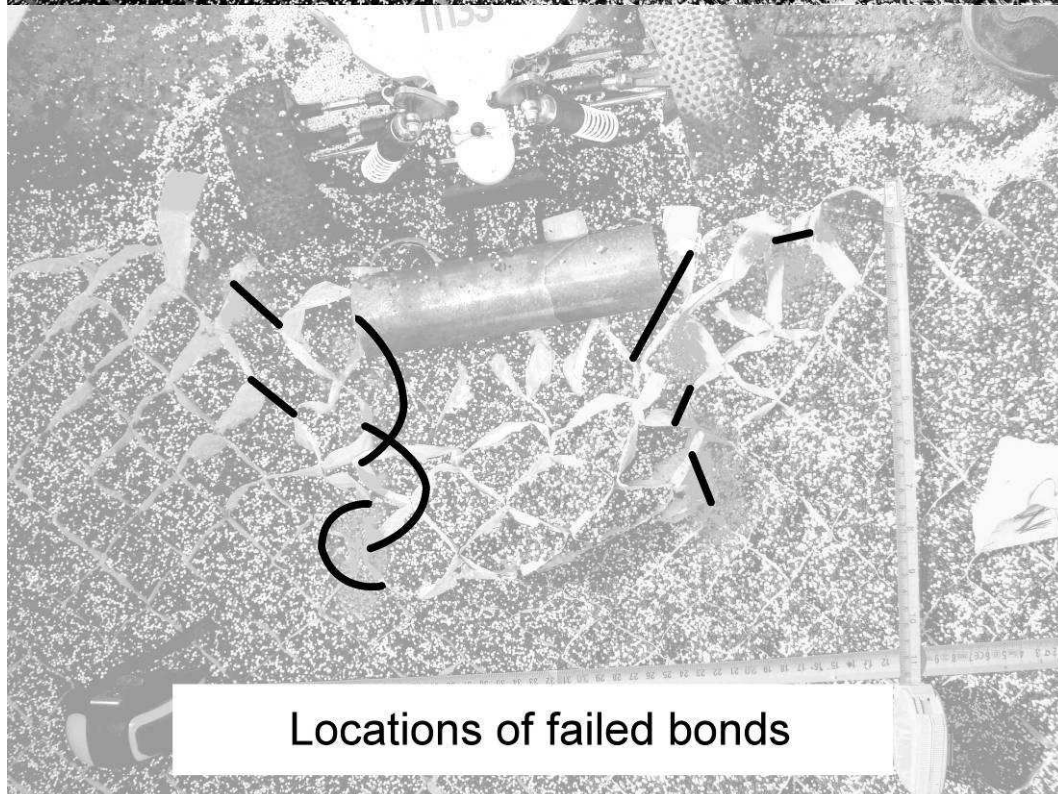
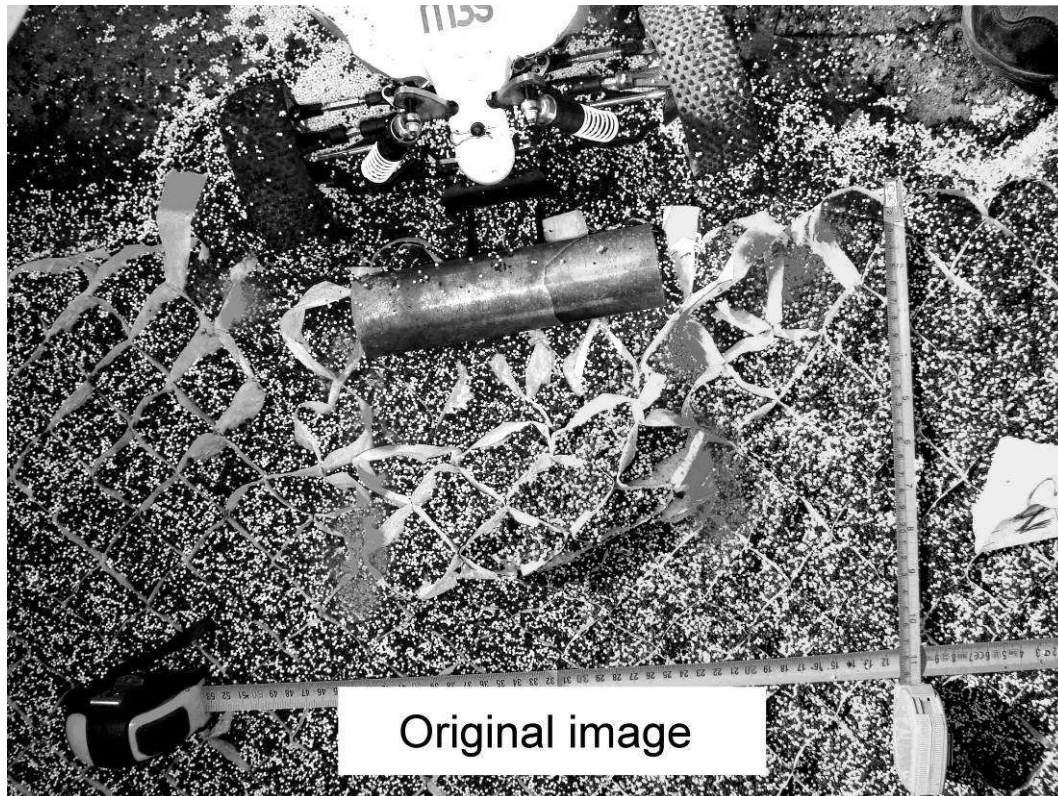
692 Fig. 5 – Deformation of the front face of the PE wall for the layer located at impact
693 level (top view)
694



695
696
697

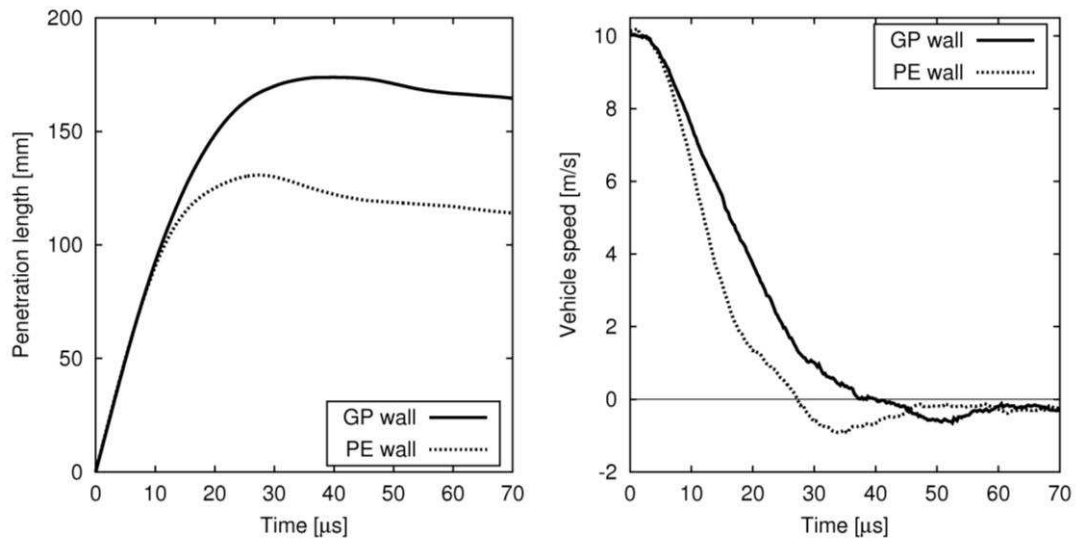
698
699

Fig. 6 – Location of broken bonds for the GP wall, in the layer located at impact level



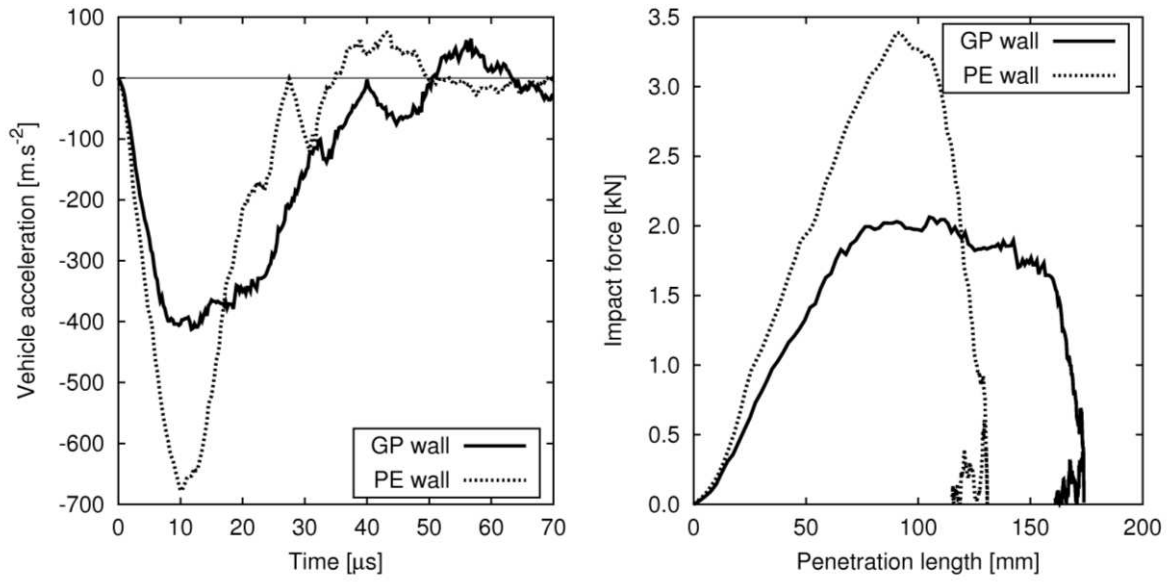
700
701

702 Fig.7 – Penetration length and vehicle speed versus time for both GP and PE walls
703



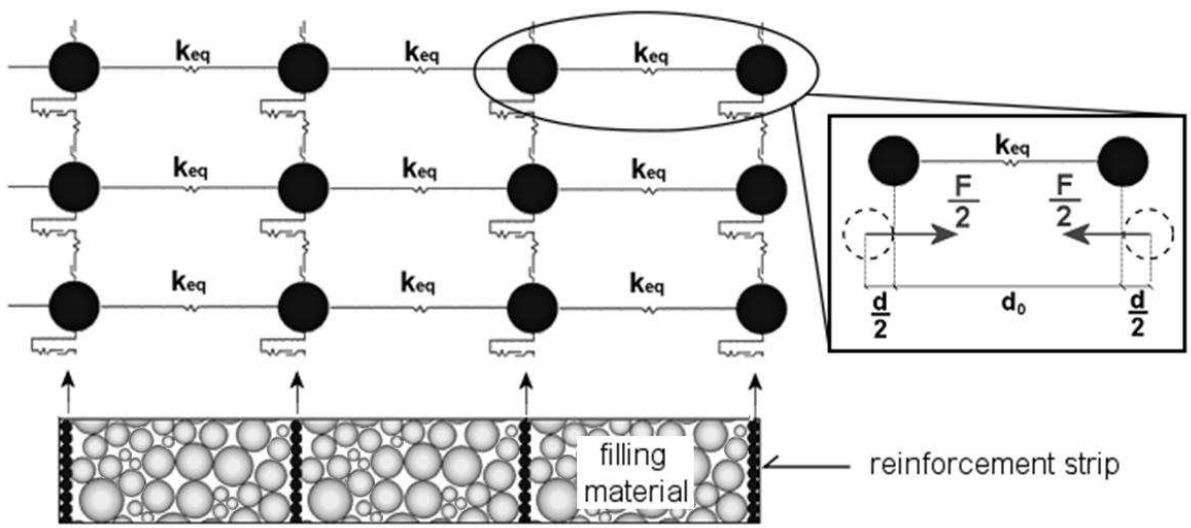
704
705

706 Fig.8 – Acceleration and unbalanced force on impacting vehicle versus time for both
707 GP and PE walls
708

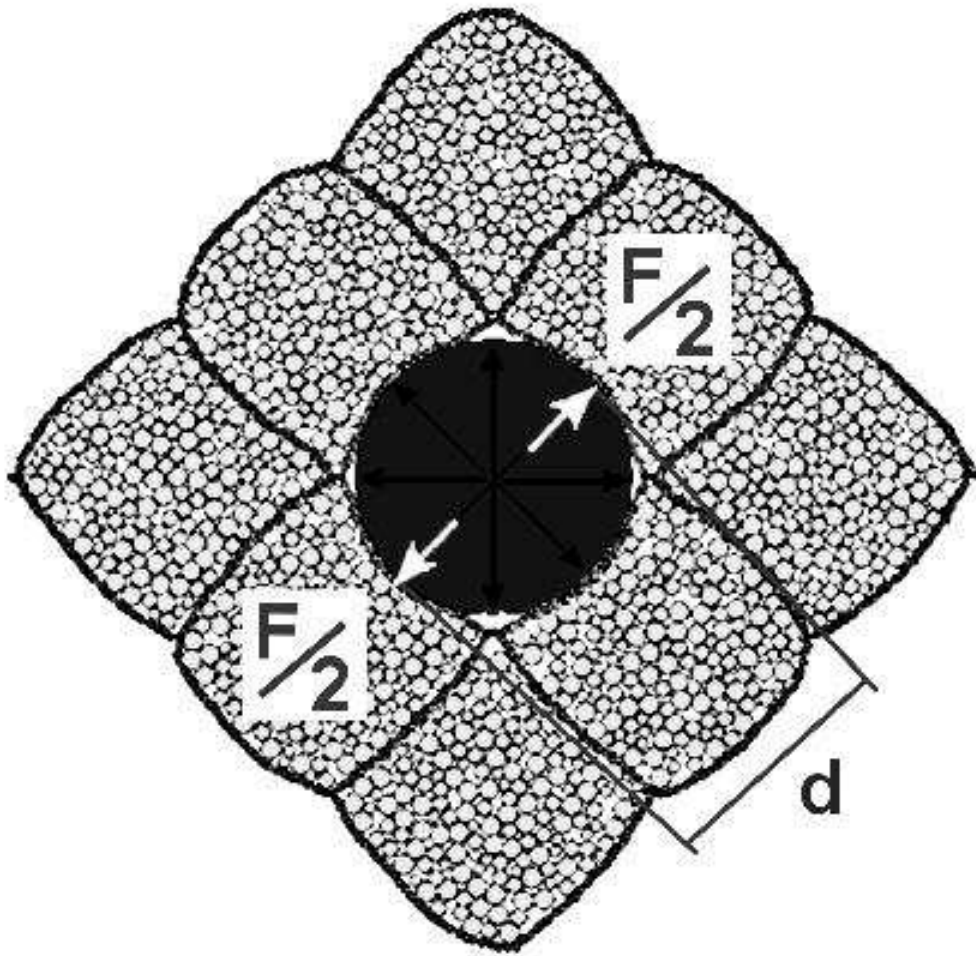


709
710

711 Fig. 9 – Diagram showing the numerical model used for the reinforcement strips
712

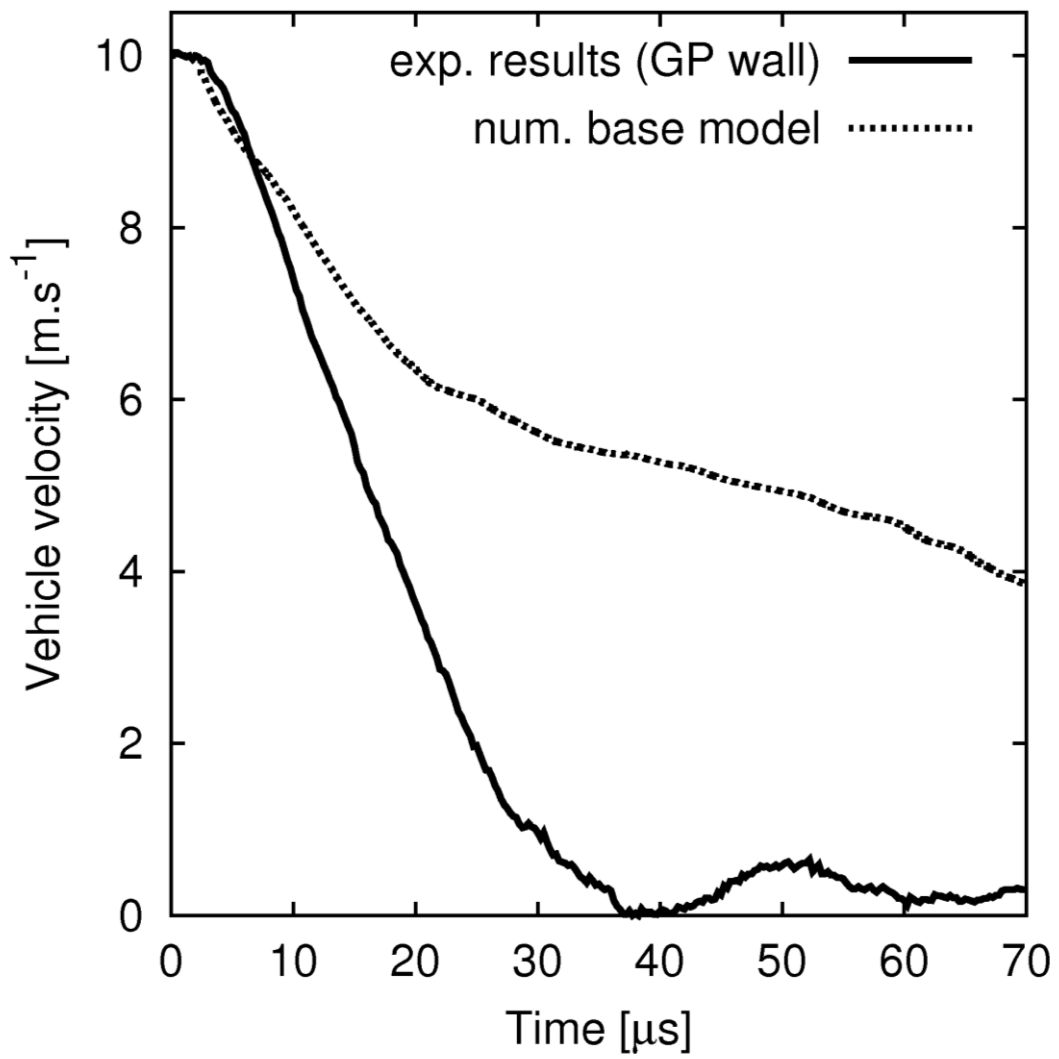


715 Fig. 10 – Diagram showing the principle of the numerical expansion test on filled cells
716



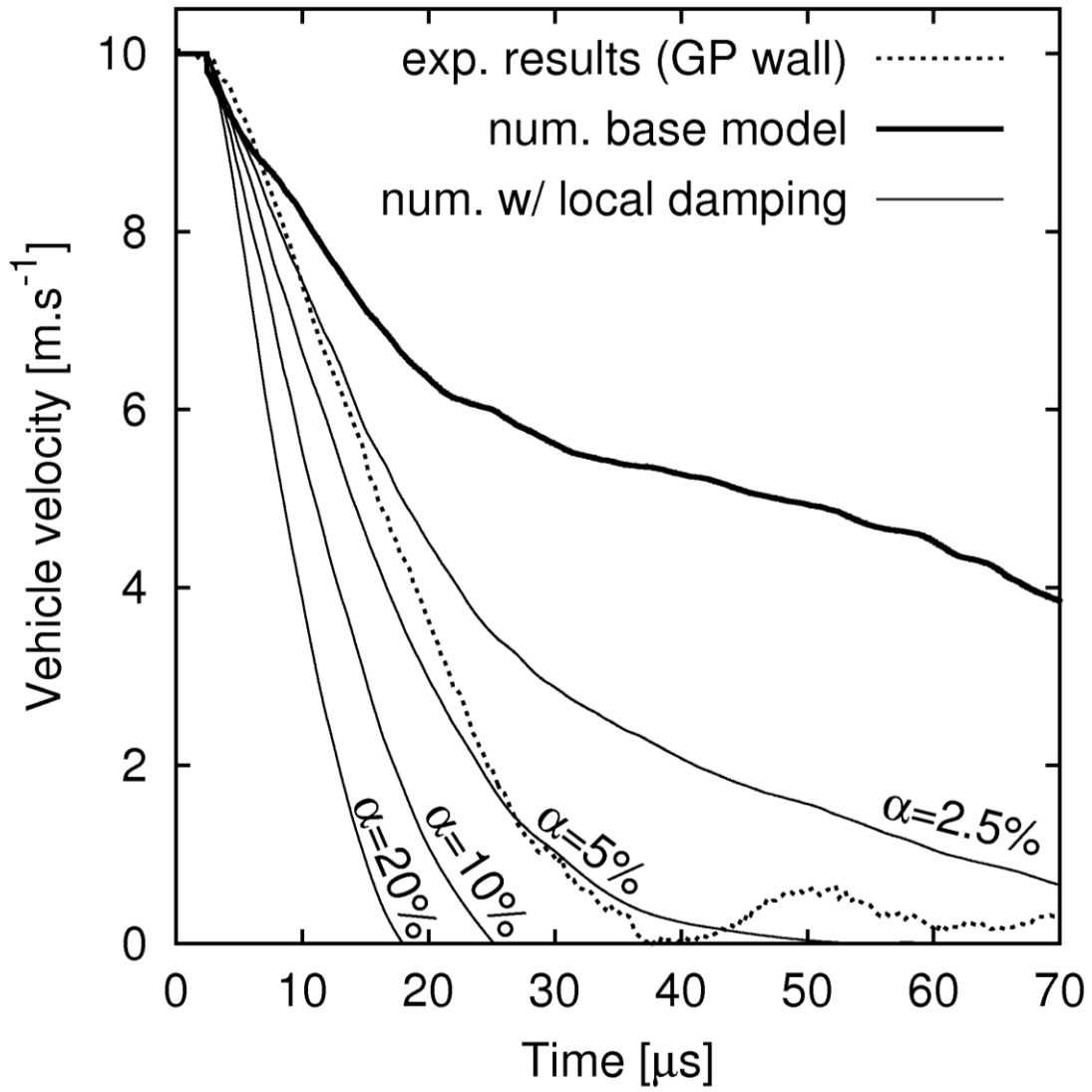
717
718

719 Fig. 11 – Comparison of vehicle velocity versus time for the experimental wall (GP)
720 and basic numerical model.
721



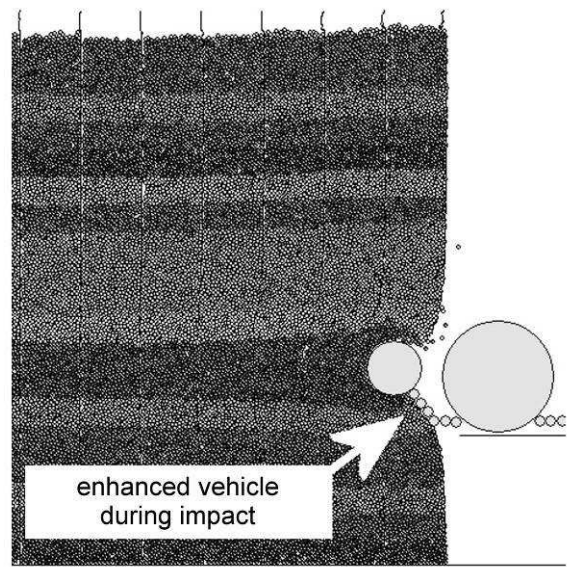
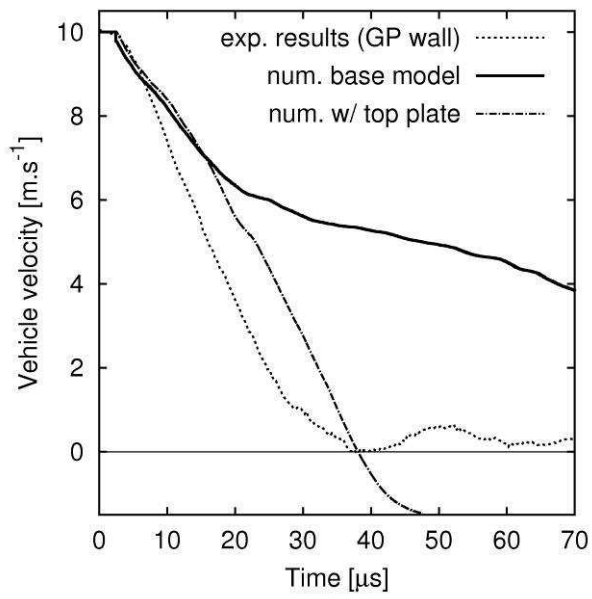
722
723

724 Fig. 12– Influence of the local damping coefficient in the basic numerical model on the
725 response of the wall in terms of vehicle velocity versus time.
726



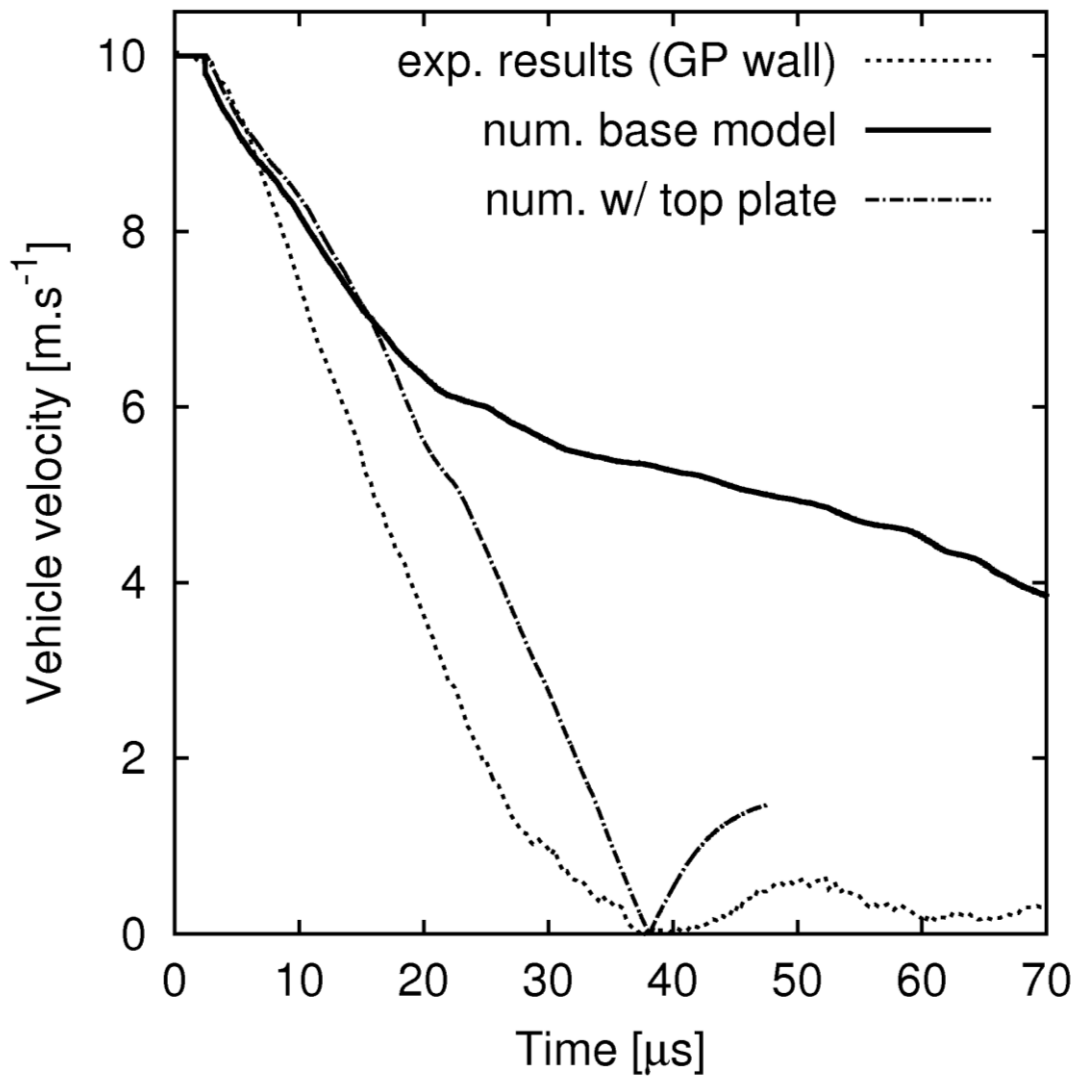
727
728

729 Fig. 13– Vehicle velocity versus time for the basic model, enhanced vehicle model and
730 experimental test.
731



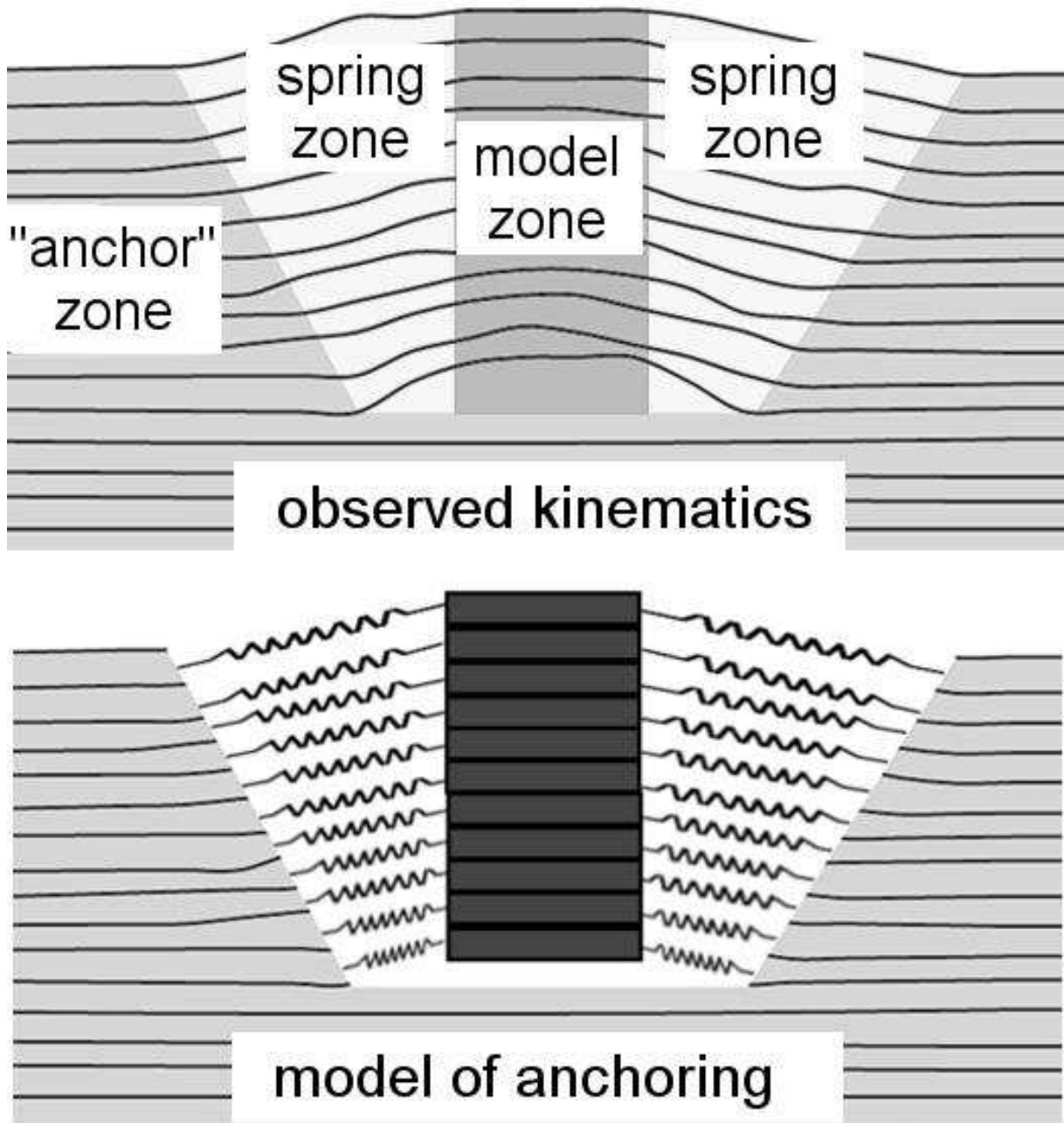
732
733

734 Fig. 14 – Vehicle velocity versus time for the basic model, top plate model and
735 experimental test.
736



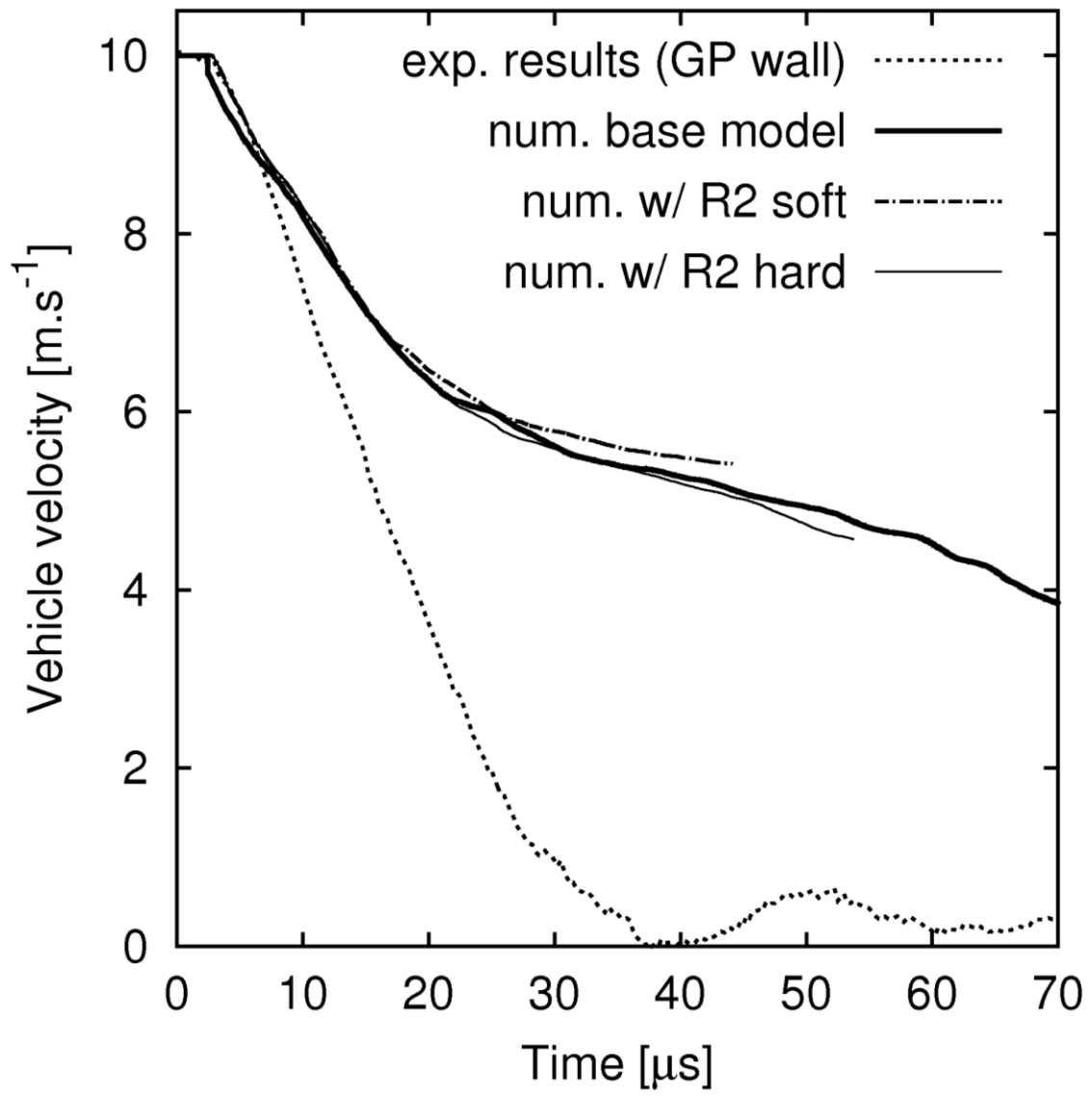
737
738

739 Fig. 15 – Enhanced model for the reinforcement strips.
740



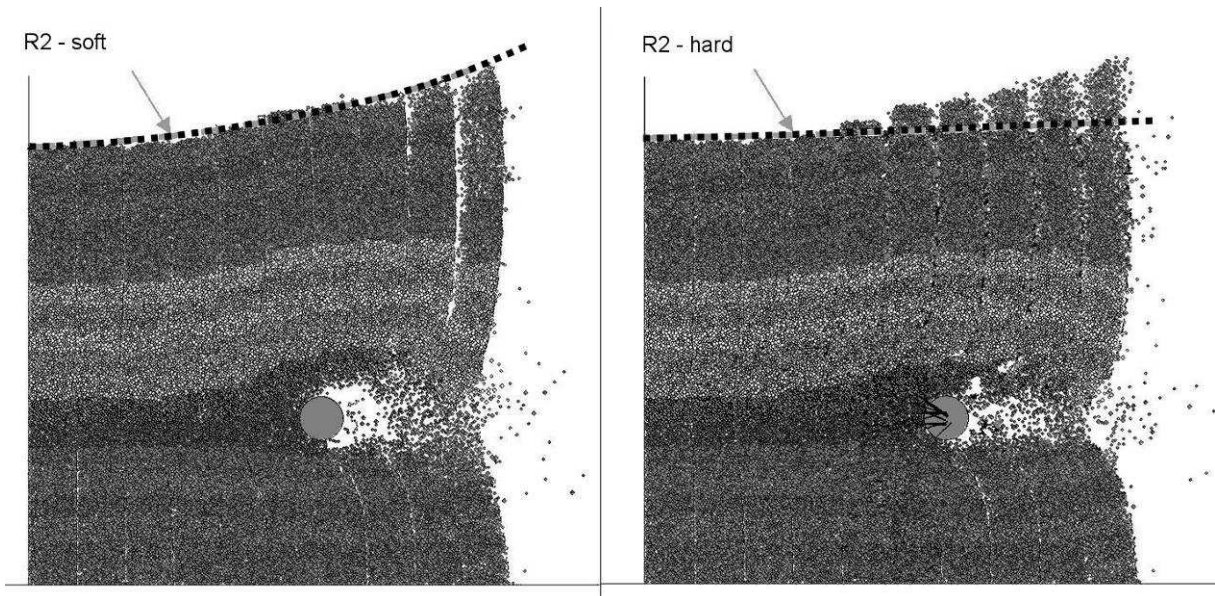
741
742

743 Fig. 16 – Vehicle velocity versus time for the experimental test, the basic numerical
744 model and the improved reinforcement models (soft and hard cases).
745



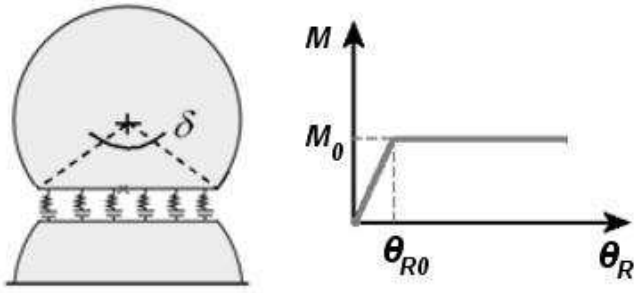
746
747

748 Fig. 17 – Cross-section of the modelled wall in the case of the improved reinforcement
749 model with soft stiffness (left) and hard-stiffness (right) springs. The dotted line
750 represents the top boundary of the reinforcement strip during impact.
751



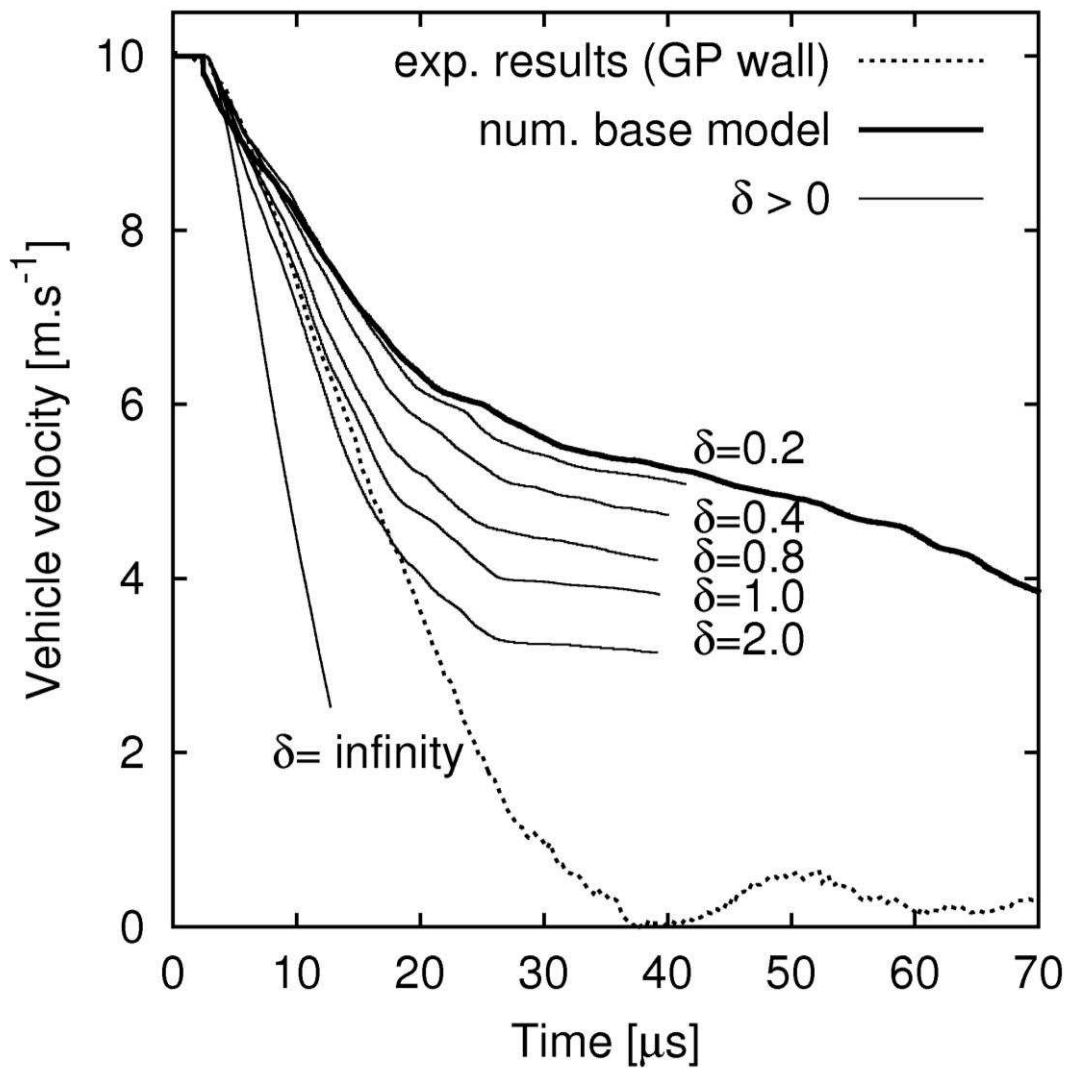
752
753

754 Fig.18 – Description of the rolling resistance model of Jiang et al. (2005)
755



756
757

758 Fig. 19 – Effect of rolling resistance on the vehicle velocity versus time for the basic
759 case and for the rolling resistance case.
760



761
762